Composites: Part A 149 (2021) 106535

Contents lists available at ScienceDirect

Composites Part A

journal homepage: www.elsevier.com/locate/compositesa

Chinese ink coated melamine foam with Joule heating and photothermal effect for strain sensor and seawater desalination

Xiang Cao [a], Hongzhong Liu [a], Jiabing Cai [a], Linhong Chen [a], Xiya Yang [b], Mingxian Liu [a,*]

[a] Department of Materials Science and Engineering, Jinan University, Guangzhou 510632, China
[b] Institute of New Energy Technology, College of Information Science and Technology, Jinan University, Guangzhou 510632, PR China

ARTICLE INFO

Keywords:
Foams
Polymer-matrix composites
Electrical properties
Optical properties/techniques

ABSTRACT

Chinese ink is a common painting material with intrinsic color of black, excellent water-dispersion stability, and proper fluidity. Herein, a conductive melamine foam (CMF) composite with various features was fabricated through a dip-coating method to assemble Chinese ink carbon nanoparticles (ICN) on the foam. The CMF combines the advantages of strain sensing, Joule heating and photothermal performance. The resistance of CMF changes rapidly upon compression or tension, so CMF is employed to monitor physiological activities. Moreover, CMF exhibits excellent Joule heating property, which is applied to sensitively detect the fingers bending action. In addition, CMF shows good photothermal performance under near-infrared light (NIR) and simulated sunlight, which is capable to carry out desalination with high evaporation rate and efficiency. This study provides a new strategy to construct a multifunctional light-absorbing and conductive device with very cheap raw materials, which shows great potentials in smart sensor and desalination.

1. Introduction

Highly sensitive sensor material is the core of the design of smart device. Generally, the good electrical conductivity and nanoscale are the basic requirements to develop a sensor, while the high signal transform efficiency is an another important parameter for smart device [1–9]. Accordingly, the materials microstructure is carefully designed for the stretchable conductive sensors, and many types of structure were explored, such as network structures [10], porous structures [11,12], wave structures [13], spiral structures [14,15], and cross-stacked structures [5]. With the development of sensitive and flexible materials, rapid responsive and high conductive sensors have been utilized in many fields such as artificial muscles, wearable electrical devices, retractable displays, motion sensors, and personal machine interfaces [3,16–18]. In recent years, pressure and electrothermal sensing were widely explored to fabricate an electrical device in intelligence sensor [19–23]. For instance, Cheng et al. developed ultrathin gold nanowires by sandwiching ultrathin gold nanowire-impregnated tissue paper between two thin polydimethylsiloxane sheets. This pressure sensor is capable to detect low pressure (13 Pa) and response rapidly (<17 ms) with high sensitivity (>1.14 kPa^{-1}) and high stability (>50,000 loading–unloading cycles) [24]. Chemical vapor deposition was implemented to make graphene growth on copper with ultrathin carbon nanotubes films as templates. This chemically hybridized film shows high conductivity and exhibits linear and reliable conductivity responses to cyclic strains. Therefore, the films act as a strain sensor to detect human finger motions with fast response and high accuracy [25]. Recently, Yang et al. prepared a stretchable graphene-polymer nanocomposite which was applied as a strain sensor using Joule heating effect. The sensor displays superior stability over 400 cycles and excellent strain sensitivity of 7.03×10^{-4} $°C^{-1}\%^{-1}$ in strain range of 0–30% [26]. Inspired by these researches, the combination of pressure sensing and Joule heating was schemed to fabricate a multifunctional wearable equipment to monitor human physiological activity.

Chinese ink, as a conventional black color material, is widely used in paint and calligraphy and plays a crucial role in Chinese cultural heritage for thousands of year [27]. Chinese ink derived from the burning product of pine tree is mainly composed of carbon nanoparticles which possess many advantages such as intrinsic color of black, good water-dispersion stability, strong adhesion to material surfaces, proper fluidity, and outstanding photothermal performance [28,29]. Therefore, ink carbon nanoparticles (ICN) can be utilized in modern high-tech fields [30,31], such as solar seawater desalination [29,32,33] and tumor treatment [34–36]. For example, Darling et al. coated ICN on the

* Corresponding author.
E-mail address: liumx@jnu.edu.cn (M. Liu).

https://doi.org/10.1016/j.compositesa.2021.106535
Received 27 March 2021; Received in revised form 14 June 2021; Accepted 20 June 2021
Available online 25 June 2021

wood and membrane stabilized by atomic layer deposition. The resulted materials behave strong and broad light-absorption property from the near-infrared (NIR) to UV regions, which exhibit superior photothermal properties and excellent evaporation performance under simulated sunlight [29]. Besides, ICN was also used as an agent in photothermal therapy for metastatic lymph nodes in rectal cancer. Interestingly, ICN shows good biocompatibility both in vitro and vivo, which can be able to eliminate the metastatic sentinel lymph nodes through NIR irradiation [28]. Furthermore, a paper-ICN cathode was fabricated and then a highly flexible Li-O_2 battery was constructed, which behaves superior mechanical strength and excellent electrochemical performances. The foldable Li-O_2 battery greatly saves the occupation space and significantly improves the volume energy density [31]. However, the related research on ICN for designing multifunctional light-absorbing and conductive device is rare in spite of its merits such as low cost, good conductivity, and superior photothermal effect.

Melamine foam is a kind of economical, technologically mature, commercial and hydrophilic porous material, which has been applied in various fields, such as sensors [37], oil–water separation [38], supercapacitors [39], photocatalysis [40], electrocatalysis [41], and flame retardants [42]. Melamine foam has many advantages of being highly porous, lightweight, highly elastic, and low thermally conductive [43]. Wang et al. fabricated a novel hybrid aerogel using melamine foam as the supporting framework while graphene nanoplatelets as the conductive path. This composite shows excellent photothermal and electro-thermal energy conversion abilities [44].

In this work, ICN was assembled to the melamine foam through a simple dip-coating method. The conductivity, piezoresistive properties, Joule heating effect, and photothermal performance of the conductive melamine foam (CMF) were studied. The resistance of CMF changes sensitively with the compression or tensile stress, so CMF was conducted to monitor small and large human activities. Furthermore, CMF exhibits excellent Joule heating property, for instance, the surface temperature of 10% CMF rises to 124.7 °C within 60 s. The elevated temperature is related to applied voltage, concentration of ICN, and working distance. The temperature changes quickly with the shape deformation which demonstrates that CMF is able to detect the fingers bending action. In addition, the outstanding photothermal performance makes CMF as a novel material in seawater desalination under NIR irradiation and simulated sunlight. This multifunctional material owns strain sensing, Joule heating and photothermal property and combines the advantages of low cost, simple preparation process, and environmentally friendliness, which shows promising potential in smart equipment and desalination.

2. Materials and methods

2.1. Materials

Zhujiang ink was purchased from Guangzhou jinjian office manufacturing plant, China. Melamine foam was obtained from Yongkang jingshang industry and trade Co., China. Ultra-pure water was originated from Milli-Q Integral Water Purification System.

2.2. The preparation of CMF composites

The solid content of raw ink was determined as 11.46%. Before the dip-coating process, the ink was diluted to a certain concentration (2%, 4%, 6%, 8%, 10%) by adding the ultra-pure water. The CMF composites were prepared according to our previous study with slight modification [45]. First, a certain amount of diluted ink was mixed with ultra-pure water in a 500 mL beaker. Then the melamine foam was soaked in above suspension, squeezed repeatedly until there was no bubble and dried at 100 °C for 6 ~ 8 h to obtain a uniform composite. During the drying process, the modified foams were turned over every half an hour to ensure even distribution.

2.3. The Joule-heating performance

Typically, the prepared composite was cut into a strip with a dimension of (length, width, thickness) 3.0 × 1.5 × 0.9 cm. Afterwards, the strip was loaded at regulated direct current (DC) power supply (GRRTTEN, APS3005S-3D) with 1.0–2.5 cm working distance and the surface temperature was recorded by an infrared imager (TiS 55, Fluke Electronic Instrument Ltd., USA). Finally, the Joule-heating performance of CMF was applied in detecting bending action of fingers.

2.4. The desalination behavior

The conductive composite was put on the seawater with the irradiation by 808 nm fiber-coupled laser (MD-III-808, Changchun New Industry Optoelectronic Technology Ltd., China) or simulate solar light (Newport, Oriel Class A, 91195A, AM 1.5 G, 100 mW/cm^2). Simultaneously, the weight loss of seawater was measured using an analytical balance and the surface temperature was detected through the infrared camera. The evaporation efficiency was calculated through the following equation:

$$\eta = \frac{mh}{Q}$$

$$h = C\Delta T + \Delta h$$

where m is the mass change rate (kg/m^2/h), C is specific heat capacity of water (4.18 J/g·K), h is the total phase change enthalpy, Δh is the liquid–vapor phase change enthalpy under the change of temperature, and Q = 1000 W/m^2 or 20,000 W/m^2 which is dependent on the light source, ΔT is temperature difference between started and final temperature.

2.5. The piezoresistive performance and sensing application

A sample with a dimension of 6 × 5 × 3 cm was compressed repeatedly and the resistance change was recorded using an electrometer (Kelthley 6514). Subsequently, the resistance change was also measured through simple deformation, such as manual compression, bending and twist. In addition, the composite was used to detect pronunciation, eye action, mouth action and nod of human.

2.6. Characterization

2.6.1. Transmission electron microscopy (TEM)

0.05 wt% ICN dispersion was dropped on the carbon membrane supported copper mesh and dried naturally at room temperature. The morphology of ICN was observed by transmission electron microscope (JEM, 1400 Flash, JEOL Ltd., Japan) at an accelerating voltage of 100 kV.

2.6.2. Scanning electron microscope (SEM)

The surface morphology of ICN and the cross-section of CMF were observed using a SEM machine (Zeiss Sigma 500). The sample of ICN was prepared by dropping ICN suspension on a glass piece and drying at 60 °C. Before observation, the surface of samples was coated with a thin gold layer. The elements distribution of C, N, O of samples was determined by energy dispersive spectrometer (EDS).

2.6.3. Atomic force microscopy (AFM)

An AFM instrument (Bioscope Catalyst Nanoscope-V, Bruker Instruments Ltd., USA) was conducted to determine the morphology of the ICN.

2.6.4. Fourier transform infrared spectroscopy (FTIR)

FTIR spectra of ICN and CMF were obtained using a FTIR spectrometer (PerkinElmer, UATR Two) at attenuated total reflection (ATR)

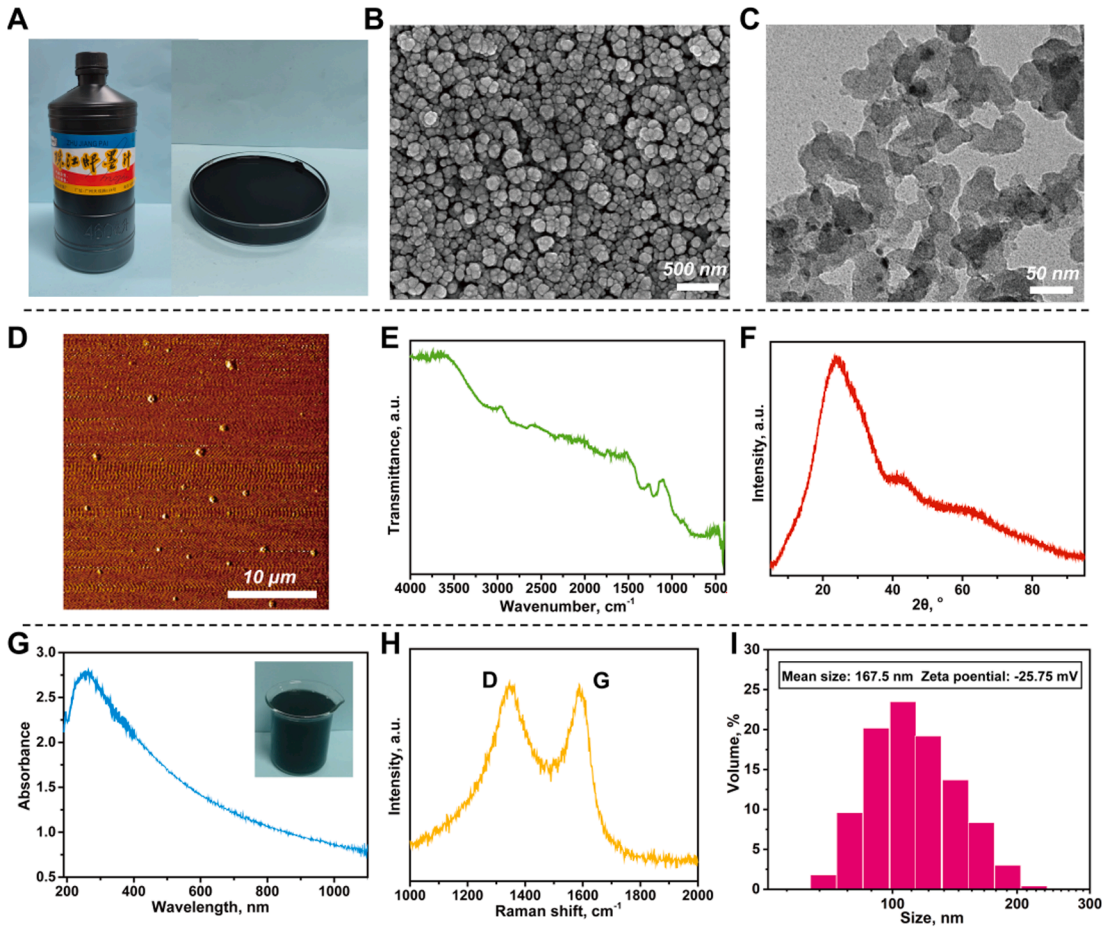

Fig. 1. (A) The photo of Zhujiang ink. Characterization of ICN: (B) SEM, (C) TEM, (D) AFM, (E) FTIR, (F) XRD, (G) UV–vis, (H) Raman, (I) particle size distribution and zeta potential.

model. The scans were taken from 4000 to 400 cm^{-1}.

2.6.5. X-ray diffraction (XRD)

The XRD pattern of ICN and CMF were determined by a Miniflex600 diffractometer, Rigaku Corp, Japan, with Cu Kα radiation at an accelerating voltage of 40 kV and the current of 40 mA. The scanning speed was set as 10°/min and scanning range was 5-90°.

2.6.6. Thermogravimetric analyzer (TGA)

The thermoanalysis curves of ICN and CMF were measured through a TGA machine (TGA2, METTLER TOLEDO Co. Ltd., Switzerland) from 50 to 700 °C at a heating rate of 10 °C/min under a nitrogen atmosphere.

2.6.7. X-ray photoelectron spectrum (XPS)

XPS machine (Thermo SCIENTIFIC K-Alpha) was performed to analyze elemental distribution and contents of ICN. The atoms of C and O were detected.

2.6.8. Zeta potential and particle size distribution analysis

The zeta potential and particle size of 0.05 wt% ICN aqueous dispersion were tested by a Zetasizer Nano ZS (Malvern Instrument Co., U.K.).

2.6.9. Raman spectroscopy

High resolution raman spectrometer (LabRAM HR Evolution) was employed to determine the raman property of ICN. The spectrum was recorded from 1000 to 2000 cm^{-1}.

2.6.10. UV–vis spectroscopy

The UV–vis spectrum of 0.05 wt% ICN aqueous dispersion was obtained by a UV–visible spectrophotometer (Evolution 201) ranged from 190 to 1100 nm.

2.6.11. Mechanical properties determination

The universal testing machine (Z005, Zwick/Roell Co. Ltd., Germany) was conducted to measure the compression performance of the foams. The dimension of the testing samples was 4.9 × 3 × 2.8 cm and the compression rate was set as 50 mm/min. On this basis, a conductive circuit was build employing a LED bulb, a composite with 10% ICN contents and the regulated DC power supply to observe the change of brightness of the bulb under compression process.

2.6.12. Density

To obtain the density of the CMF, the weight and volume of samples must be measured by an analytical balance (readable 0.0001 g, ME204E, METTLER TOLEDO Co. Ltd., Switzerland) and digital caliper, separately. Each group should be tested five times. The density was calculated by the following equation.

$$\text{Density} = \frac{m}{lwh}$$

where m, l, w, and h are the mass, length, width, and height of the samples, respectively.

2.6.13. Porosity

The weight and size of CMF were measured firstly. Afterwards, the samples were soaked in absolute ethanol for 24 h at room temperature.

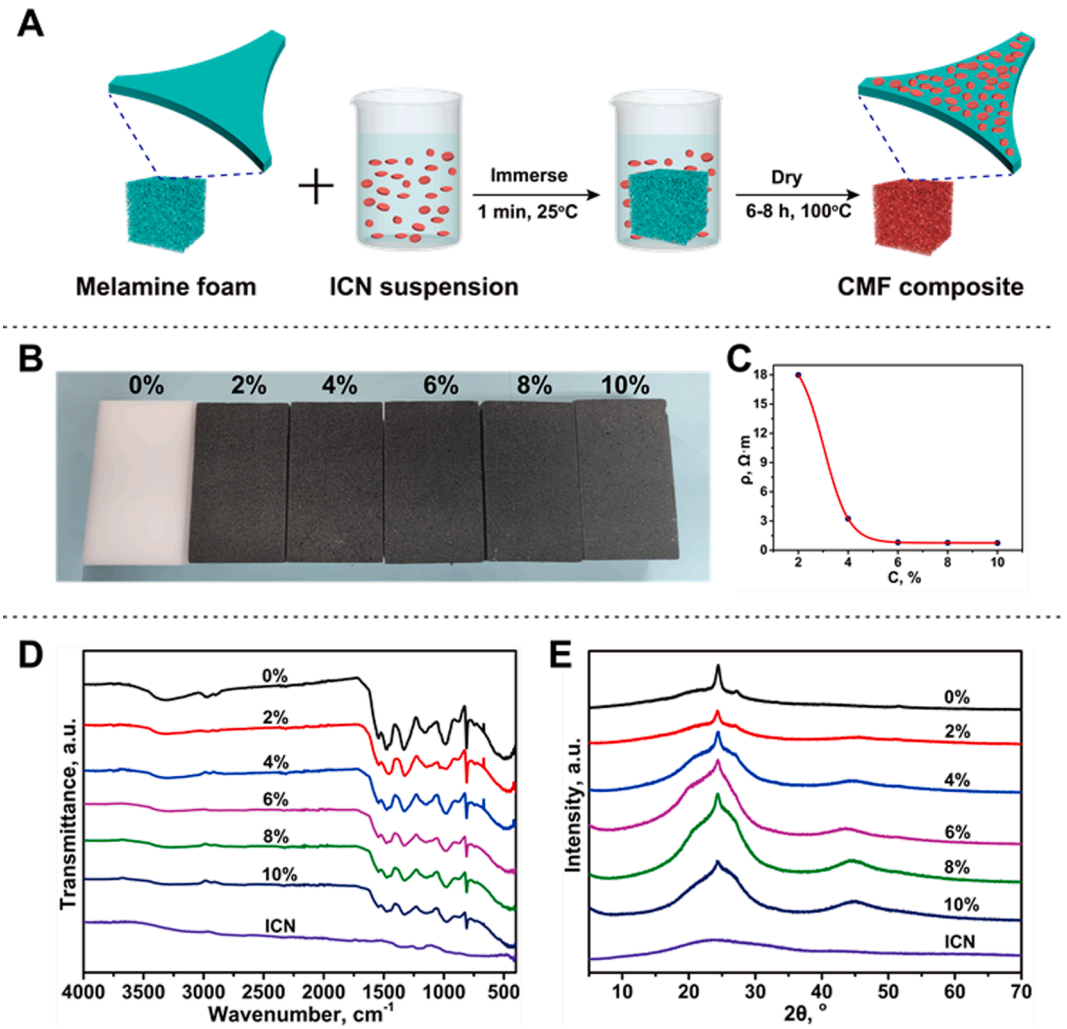

Fig. 2. (A) Schematic illustration for the preparation process of the CMF. (B) The photo, (C) resistivity, (D) IR, and (E) XRD of CMF with different ICN contents.

The samples were taken out and weighted ultimately. Each group should be tested for five times. The porosity was calculated by the following equation.

$$\text{Porosity} = \frac{m_2 - m_1}{\rho l w h} \times 100\%$$

where m_2 is the weight of the samples after immersing in ethanol absolute. ρ is the density of absolute ethanol. m_1, l, w, and h are the mass, length, width, and height of the samples at initial state, respectively.

3. Results and discussions

3.1. Characterization of ICN

Chinese ink carbon nanoparticles (ICN) may possess excellent conductivity and photothemal performance similar to carbon black and carbon nanotubes, so we performed a series of characterizations firstly. Fig. 1A displays appearance of Zhujiang ink and the morphology of ICN was then characterized by SEM, TEM and AFM (Fig. 1B, C and D). It is clear that ICN exists in the form of small sphere-like aggregates composed by amorphous sheets, whose size ranges from 20 to 60 nm. The FTIR spectrum (Fig. 1E) demonstrates no strong absorbance peaks due to the absence of the chemical groups of ICN. However, the peaks in the range of 1100–1500 cm^{-1} is assigned to the D-band of the ICN observed in Raman spectra [46]. XRD pattern of ICN in Fig. 1F shows a broad peak at about 25° which is assigned to the carbon crystal plane (0 0 2). This typical characteristic agrees with graphitic carbon materials [31]. UV–vis analysis of diluted Chinese ink was conducted (Fig. 1G) and the result indicates that the absorption peak at 255 nm is assigned to the electronic conjugation in graphite [47]. Raman spectrum of ICN (Fig. 1H) shows the D band (1343 cm^{-1}) and G band (1587 cm^{-1}), which confirms the components of both amorphous carbon and graphene sheet-like structure in ICN [48]. The average particle size by DLS method and zeta potential of ICN are 167.5 nm and −25.75 mV (Fig. 1I). The larger particle size can be attributed to the slight aggregation of carbon nanoparticles. Moreover, the high surface negative potential of ICN indicates that the ink possesses excellent water-dispersion stability. XPS scanning was conducted on ICN to detect the elements. As showed in Fig. S1A and B, the survey and the high-resolution spectra of XPS of nitrogen and oxygen element suggest that the components of ICN are O and C. C 1 s and O 1 s of the ICN appear at 285.08 eV and 533.08 eV, respectively. Carbon content in ICN is 83.76%, which implies it is a high conductive and photothermal nanomaterial.

3.2. Characterization of CMF

In virtue of the excellent property, ICN was coated on melamine foam surfaces to prepare conductive melamine foam (CMF). As displayed in Fig. 2A, the foam was soak in the different concentration ink solution and squeezed repeatedly, then it was dried at 100 °C to obtain a series of modified foam (Fig. 2B). The resistance of CMF was determined and displayed in Fig. 2C. The resistance declines as the increase of ICN

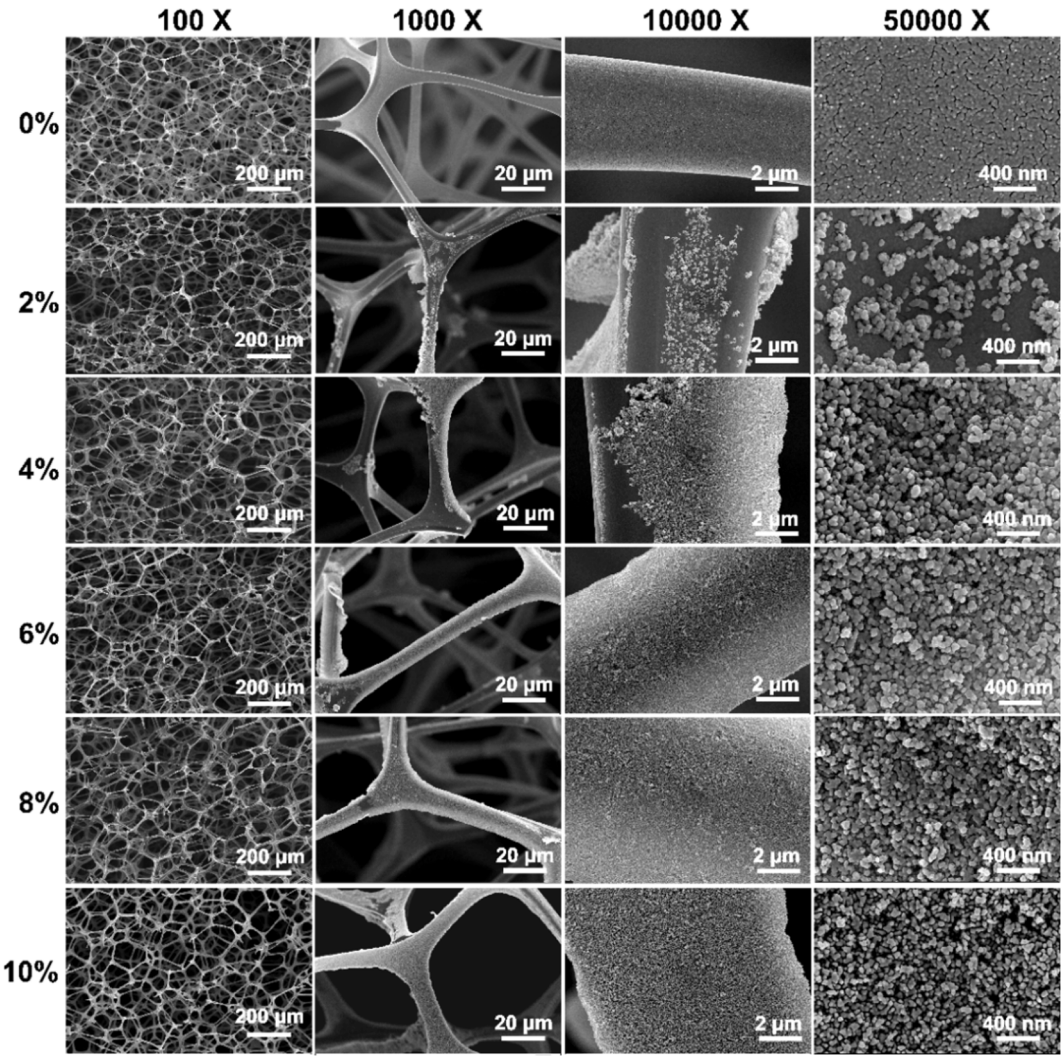

Fig. 3. SEM images of CMF with different ICN contents.

contents, which is due to the incorporation of the ICN. FTIR and XRD measurement of CMF were performed and the results are showed in Fig. 2D and E, respectively. The characteristic absorption peaks of N-H stretching vibration (3343 cm^{-1}), C-H stretching vibration (2968 and 2897 cm^{-1}), C-N rings (1171, 1335, 1469, 1550 cm^{-1}) and N-H bending vibration (812 cm^{-1}) are ascribed to the functional group of the foam [49]. The characteristic absorption peaks change slightly and only intensity decreases due to the introduction of ICN on the foam surfaces. In Fig. 2E, it is clear that the XRD peaks of the pure foam are located at 24.42° (0 0 4) and 27.12° (12$\bar{1}$). After introduction of ICN, the peak at 24.42° gets broad because of influence of the carbon crystal plane (0 0 2) [50].

Fig. S2A and B compare density and porosity of CMF. The density of CMF increases while the porosity decreases slightly as the increase of ICN content. The pure foam has lowest density of 9.73 mg/cm^3, while the density of 10% CMF is 51.52 mg/cm^3. This can be attributed to more ICN in same volume. The porosity of pure foam is 95.33%, but the 10% CMF still maintain a high value of 82.85%. So, although introduction of many ICN on the foam surfaces, the porosity of the foam is not seriously damaged. The thermal stability of CMF with different ICN content was determined and the TGA curves and DTG curves of CMF and ICN are compared in Fig. S2C and D. From 50 to 700 °C, the weight loss of ICN is 25.69% which is ascribed to volatilization of absorbed and bound water. It suggests that ICN possesses excellent thermal stability. The weight loss of pure foam is 87.74% due to the main decomposition process of foam from 360 °C to 430 °C [51]. After introducing ICN, the TGA curves show that the residual of CMF is more than that of pure foam, which can be attributed to the high content of ICN. It also demonstrates that the thermal stability of CMF is enhanced significantly. The ICN content in the foam can be calculated from the difference between residual of CMF and pure foam. The ICN content in the foam of 2%, 4%, 6%, 8% and 10% CMF is calculated as 28.13%, 37.67%, 43.94%, 53.57% and 58.63%, respectively.

The pore structure of CMF was observed using a SEM machine (Fig. 3). It is clear to see that CMF is composed of massive pores which has an average diameter of approximate 200 μm and the pore wall is thin and narrow. As the ICN content increases, the pore walls are firmly attached with more and more ICN via Van der Waals forces and hydrogen bonds interactions. The morphology of the ICN on the foam is same to the pristine ICN, suggesting no structure change during the dip-coating process. Chinese ink possesses outstanding adhesion ability due to their small dimensions and high surface activities, so ICN is capable to bond on foam tightly through physical adsorption. The difference of CMF with varied ICN content is significant, and the energy dispersive spectrometer (EDS) was used to investigate element component of C, N, and O (Fig. S3). It shows that carbon content of 10% CMF is 82.78% which is significantly higher than that of 0% CMF (43.66%). Therefore, coating of ICN on the polymer foam can lead to a uniformly conductive composite.

The compression property determination of CMF was conducted

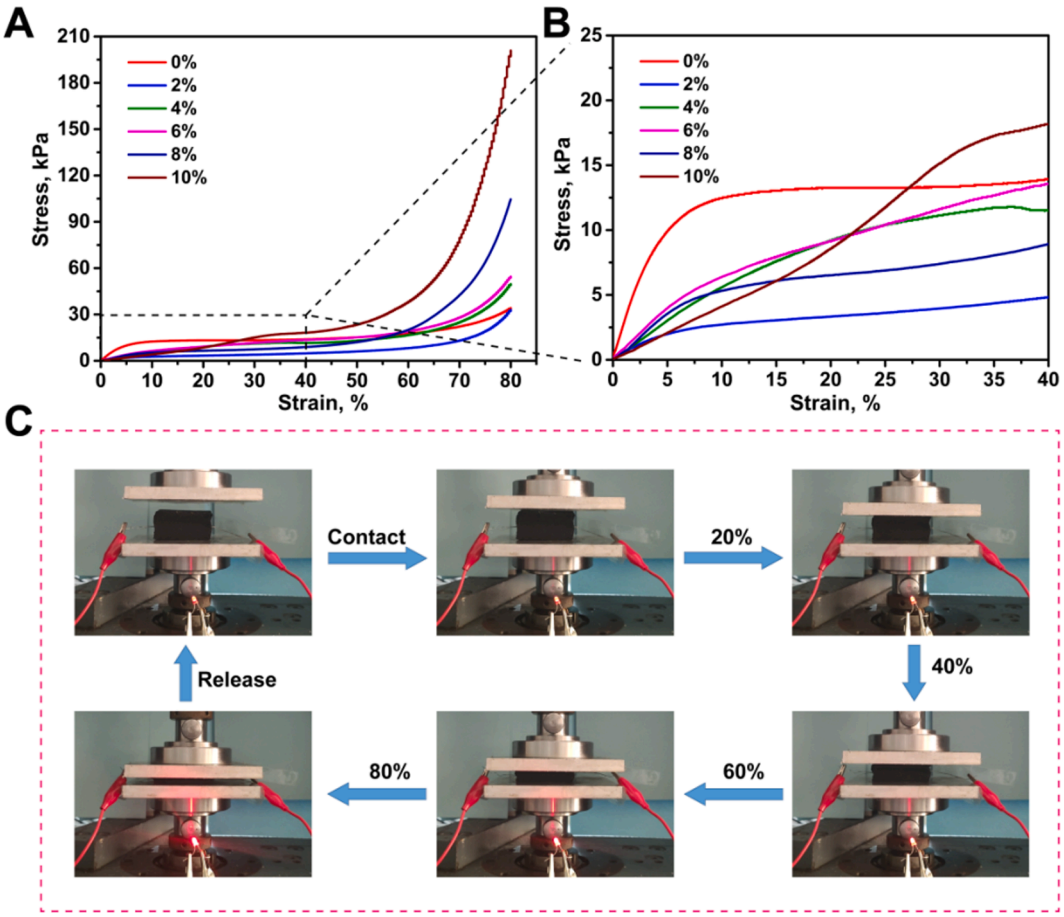

Fig. 4. (A), (B) Compressive stress–strain curves of CMF with different ICN contents. (C) The change of brightness of the bulb during the compression of 10% CMF.

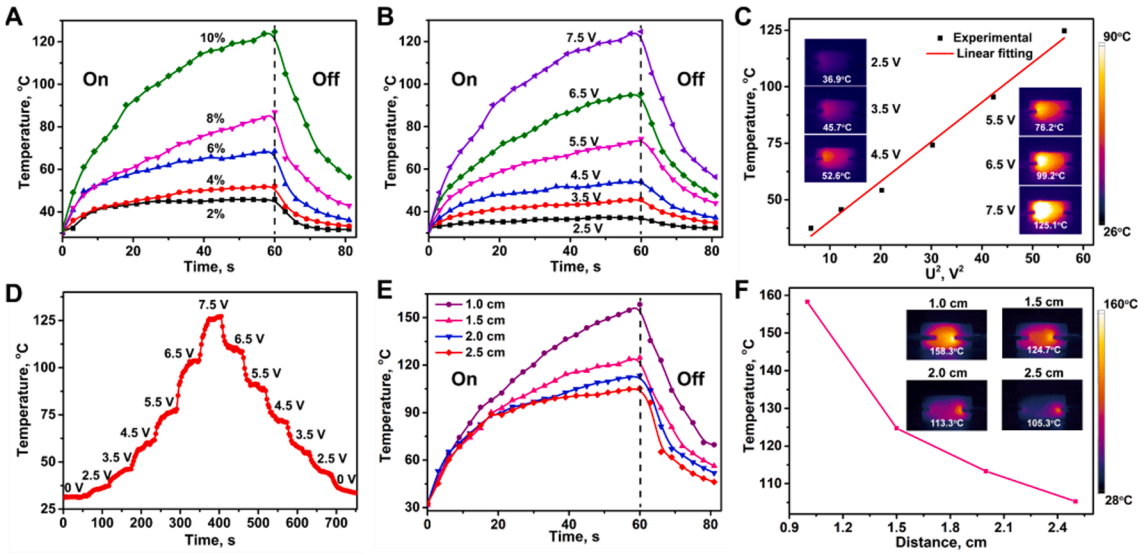

Fig. 5. Temperature changes of (A) CMF with different ICN contents under 7.5 V voltage and (B) 10% CMF under various voltage. (C) The relationship between temperature and voltage of the 10% CMF and its infrared thermal images. (D) Temperature curves of the 10% CMF under continuous voltage change and (E) different working distance at 7.5 V voltage. (F) The relationship between temperature and working distance of 10% CMF and its infrared thermal images.

using the universal testing machine. It can be seen from Fig. 4A and B that the compressive strength at 80% strain of 10% CMF is 200.9 kPa which is 5.88 multiples of that of pure foam (34.2 kPa), but the compressive strength (13.3 kPa) at 20% strain of pure foam is high than all percentage of CMF. It demonstrates that the introduction of ICN endows the foam enhanced compression resistance at high strain but the flexibility of CMF would be reduced. This phenomenon is ascribed to the increase in density and the decrease in porosity of CMF by the rigid ICN. In order to study the conductivity of CMF under different compression deformation, a conductive circuit was build employing a LED bulb by

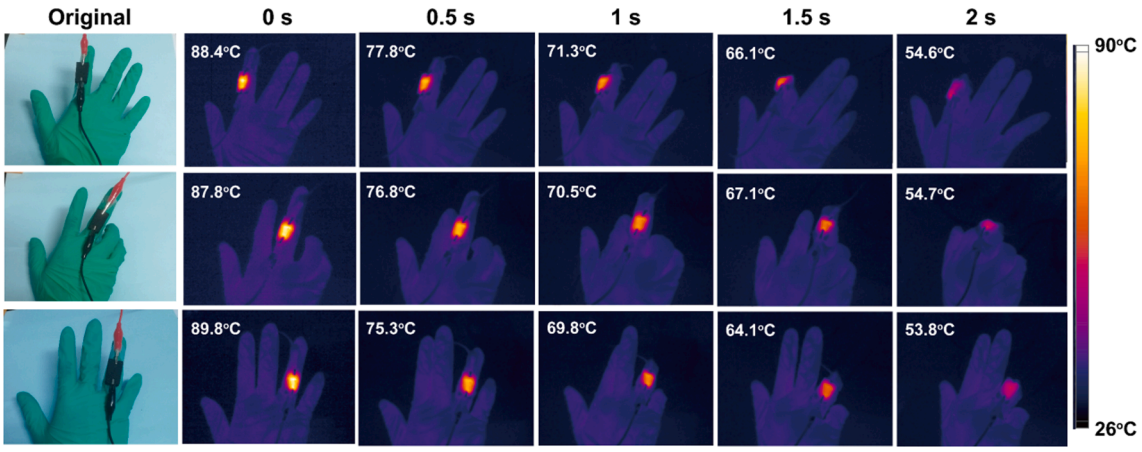

Fig. 6. The relationship of finger action and the temperature change for the 10% CMF in wearable devices.

linking a foam with 10% ICN content with the DC power. It is convenient to observe the change of brightness of the bulb under compression process. In Fig. 4C, the bulb presented weak red light after connecting the circuit and got brighter gradually under compression. It suggests that the conductivity of CMF gets better with increasing strain due to tighter conductive network upon compression.

3.3. Joule heating performance

Considering the good electrical conductivity of CMF, the prepared CMF material can be used as high-performance Joule heaters with excellent thermal management performances. Fig. 5A and B show temperature changes of CMF with different ICN contents under 7.5 V voltage and the CMF with 10% ICN content under various voltage. As the content of ICN and the voltage increase, the surface temperature at 60 s enhances significantly owing to the generation of greater Joule heat which is caused by decreases of resistance and the higher current. For example, the surface temperature of 10% CMF at 7.5 V voltage quickly reaches 124.7 °C within 60 s while that of 2% CMF only is 45.8 °C. Similarly, the surface temperature of 10% CMF under 2.5 V voltage is only 37.0 °C within 60 s, while it rises to 95.5 °C under 6.5 V. Fig. 5C gives the experimental data and linear fitting of surface temperature versus U^2 at 60 s. A favorable linear relationship between surface temperature and voltage square of the CMF is identified, which is consistent with relevant reported in previous studies [52,53]. And the infrared thermal images also support this result. This can be explained by that the equation of heat energy $Q = U^2t/R = cm\Delta T$ (Q = heat energy (J); U = voltage (V); t = time (s); R = resistance (Ω); m = mass of a substance (kg); c = specific heat (J/kg·K)), which suggests that the temperature rising (ΔT) is proportional to the U^2.

Fig. 5D illustrates that the surface temperature of CMF can be adjusted by change the output voltage, which may be attributed to the high sensitivity of generated Joule heat. Fig. 5E and F demonstrate that the temperature rising is related to the working distance. As working distance gets shorter, the CMF behaves higher surface temperature. For example, the surface temperature of 10% CMF with 2.5 cm working distance under 7.5 V voltage within 60 s is 105.3 °C while the value with 1.0 cm is 158.3 °C. The superior thermal management performance of CMF shows great potential in wearable device. Therefore, 10% CMF was further employed to detect the bend action of fingers. As displayed in Fig. 6, the surface temperature of CMF changed quickly within short time of 2 s during bending and recovery of the finger. For instance, the temperature of CMF is 88.4 °C when index finger is straight and the temperature decreases to 54.6 °C rapidly while the finger is at bent state. The middle and ring finger attached by the CMF also display the quickly changed temperature phenomenon. It indicates that CMF is capable of using as a strain sensor for wearable device. Graphene-polymer nanocomposites were reported in previous study, which shows superior sensing ability through Joule heating effect [26]. However, the fabricated process of materials is complicated and raw materials are expensive compared with the present research.

3.4. Seawater desalination

The photographs and photothermal images of calligraphy and CMF are shown in Fig. S4, and it is visible that the ICN and CMF possess excellent photothermal performance under sun which may be applied in seawater desalination. First, 808 nm laser was employed as the light source to simulate seawater desalination process. Fig. 7A presents the photothermal images and it is clear that the surface temperature is related with concentration of ICN and laser power. Fig. 7B and C show the surface temperature change of the CMF with different ICN contents and laser power. The surface temperature rises sooner and higher as the ICN contents and power increase. For example, when samples are irradiated by 808 nm laser (2 W/cm^2), the temperature of 10% CMF increases to 86.2 °C within 1 min and further rises to 106.7 °C within 15 min, whereas control group (pure water) and the pure foam only reach 30.8 °C and 45.2 °C within 15 min, respectively. The temperature rising is proportional to the laser power, and the low power leads to limited temperature rising. For example, the temperature of 10% CMF only reaches 33.9 °C within 15 min under 0.5 W/cm^2 irradiation.

We employed simulated sun light to carry out the seawater desalination. Fig. S5 shows the photo of desalination device under one sun light. The surface temperature of 10% CMF increases to 42.3°C from 28.8°C within 60 min. The laser with 2 W/cm^2 power was used to determine the mass loss of seawater. As displayed in Fig. 7D, 10% CMF exhibits quicker and more mass loss of seawater than other groups, and higher ICN percentage of CMF performs better capability as expected. The mass loss of blank, 0%, 2%, 4%, 6%, 8%, and 10% CMF are 0.20, 0.58, 2.13, 2.25, 2.54, 3.05, 3.26 kg/m^2, respectively. The evaporation rate and efficiency are shown in Fig. 7E which demonstrate an increasing trend with ICN concentration. The evaporation rate of 10% CMF is 3.26 kg/(m^2·h) which is much higher than that of control (0.20 kg/(m^2·h)) and 0% CMF (0.56 kg/(m^2·h)). Specifically, the evaporation efficiency of 10% CMF is 74.71% which is much higher than that of control (0.11%) and 0% CMF (3.04%). The porous structure of melamine foam offers abundant water channels, and the excellent photothermal effect of the carbon nanoparticles can convert light energy into heat energy with high efficiency. These results indicate that CMF possesses superior photothermal conversion capability, which support the prepared CMF is a good alternative for desalination.

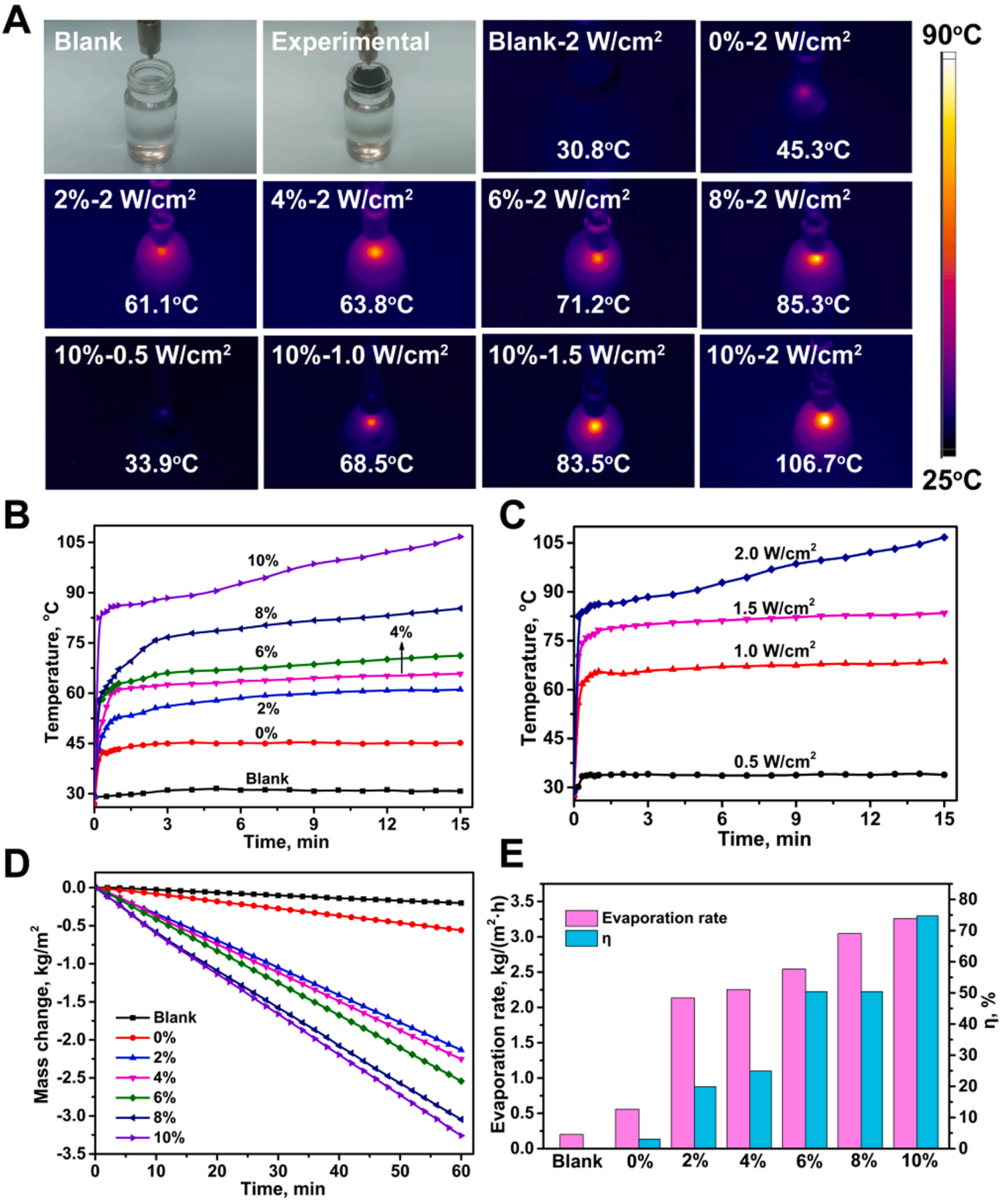

Fig. 7. Seawater evaporation behavior the 10% CMF under irradiation of 808 nm laser. (A) Photothermal images; Temperature change of CMF with (B) different ICN contents and (C) various laser power. (D) Mass change versus time and (E) evaporation rate and evaporation efficiency.

3.5. Piezoresistive sensor

Fig. 8A shows the relation between conductivity of CMF and contents of ICN, which demonstrates that the conductivity of CMF increases with ICN content. The conductivity increases sharply when percentage of ICN improves from 4% to 6% (0.31–1.24 S/m). This suggests that the conductive network threshold occurs at 6% ICN treated foam sample. The 10% CMF was employed to conduct the following work because of its high conductivity. The resistance of CMF is very sensitive to compression strain (Fig. 8B), and the R/R_0 of CMF under 0%, 20%, 40%, 60% and 80% strain is 1.0, 0.90, 0.74, 0.54 and 0.39, respectively. The relationship between R/R_0 and strain is also displayed in Fig. 8C. The tighter conductive network of CMF is obtained by compression, larger resistance change ratio of CMF is occurred. The resistance of CMF exhibits good repeatability and stability after 1000 s compression-recovery cycles with slightly changed resistance (Fig. 8D). It is worth noting that the R/R_0 shifts to high value in the later period, which is due to that the ICN conductive network is destroyed or deformed partly caused by the long period of compression cycle. Since the damage of ICN network is unable to be self-repaired, the baseline offset is commonly found in the recycle curves [17,54].

The CMF was then used to detect bending action of finger and wrist, and the R/R_0 curves are displayed in Fig. 8E and F. When the index finger bends, the resistance of CMF appears to significantly increase due to the stretching of the conductive network. The resistance recovers to its original level while the finger is straightened, which arises from the

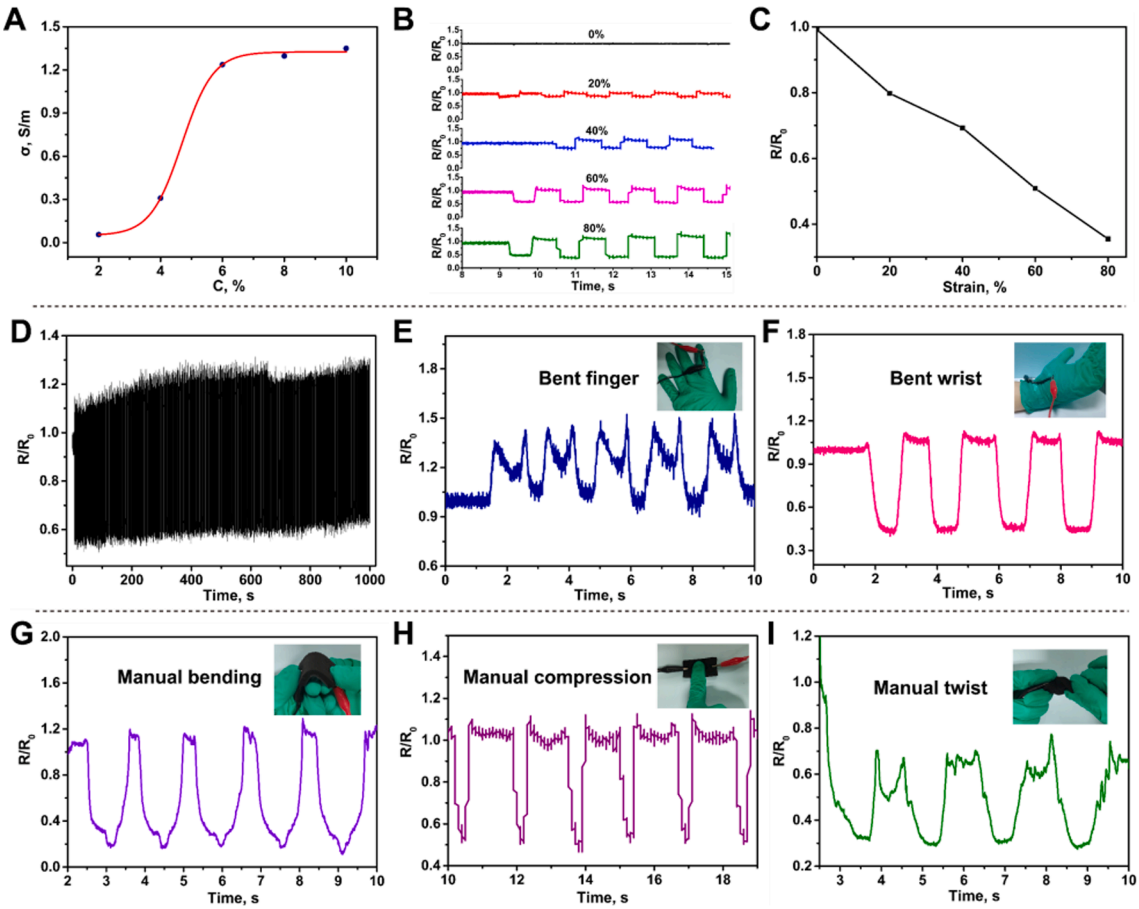

Fig. 8. (A) Conductivity of CMF with different ICN contents. (B) Resistance change and (C) relationship with the deformation of 10% CMF under various deformation and (D) fatigue resistance. (E-I) Resistance change of the 10% CMF under different actions.

reconstruction of the ICN network in the CMF. The signal produced by the bending action of finger maintains a high degree of similarity. It demonstrates that CMF behaves fast response and stable electrical signal in detection of body movement of human. Furthermore, the CMF was fixed to the volunteer's wrist joint and the real-time signal of resistance was recorded under repeated bending-stretching movement of the wrist. Fig. 8F illustrates that the R/R_0 reduces while bending the wrist, which is caused by the squeeze of CMF. Similarly, the action of manual bending, manual compression and manual twist were conducted on the CMF, and the corresponding curves with different shape are recorded in Fig. 8G, H and I. The decreases of R/R_0 are also due to the squeeze of CMF which leads to the decline of resistance. In additon, the CMF are capable to monitor human activities such as pronunciation, eyes action, mouth action, nodding and finger bending (Fig. S6), which can be applied in the manufacture of smart device in healthcare equipment.

4. Conclusions

We present a facile dip-coating method to prepare CMF composites using cheap and abundant Chinese ink. The CMF combines the merits of strain sensing, Joule heating and photothermal property. CMF exhibits excellent electric heating property, for instance, the surface temperature quickly improves to 124.7 °C within 60 s. The surface temperature of CMF is strongly related to applied voltage, concentration of ICN, and working distance, and also changes rapidly with the deformation of CMF. Taking the advantage of the accurate temperature change, the CMF can detect the fingers bending action sensitively. CMF shows good photothermal performance and is able to perform desalination under NIR and simulated sunlight with good evaporation rate and evaporation efficiency. In addition, the resistance of CMF changes rapidly and sensitively with the compression or tensile deformation, therefore they are capable to monitor human activities such as pronunciation, eyes action, mouth action, nodding and finger bending. This work offers a rapid, simple and cheap strategy to design multifunctional sensor materials, which shows promising applications in intelligent product and seawater purification.

CRediT authorship contribution statement

Xiang Cao: Validation, Formal analysis, Investigation, Data curation, Writing - original draft. **Hongzhong Liu:** Software, Investigation. **Jiabing Cai:** Software, Investigation. **Linhong Chen:** Software, Resources. **Xiya Yang:** Resources, Methodology. **Mingxian Liu:** Conceptualization, Methodology, Supervision, Writing - review & editing.

Declaration of Competing Interest

The authors declare that they have no known competing financial interests or personal relationships that could have appeared to influence the work reported in this paper.

Acknowledgements

This work was financially supported by the National Natural Science Foundation of China (52073121), Science and Technology Planning Project of Guangdong Province (2019A050513004), and the Fundamental Research Funds for the Central Universities (21619102).

Appendix A. Supplementary material

Supplementary data to this article can be found online at https://doi.org/10.1016/j.compositesa.2021.106535.

References

[1] Cheng Y, Wang R, Sun J, Gao L. Highly conductive and ultrastretchable electric circuits from covered yarns and silver nanowires. ACS Nano 2015;9(4):3887–95.
[2] Yi F, Lin L, Niu S, Yang PK, Wang Z, Chen J, et al. Stretchable-rubber-based triboelectric nanogenerator and its application as self-powered body motion sensors. Adv Funct Mater 2015;25(24):3688–96.
[3] Ren J, Wang C, Zhang X, Carey T, Chen K, Yin Y, et al. Environmentally-friendly conductive cotton fabric as flexible strain sensor based on hot press reduced graphene oxide. Carbon 2017;111:622–30.
[4] Shi G, Zhao Z, Pai JH, Lee I, Zhang L, Stevenson C, et al. Highly sensitive, wearable, durable strain sensors and stretchable conductors using graphene/silicon rubber composites. Adv Funct Mater 2016;26(42):7614–25.
[5] Yu Y, Luo S, Sun L, Wu Y, Jiang K, Li Q, et al. Ultra-stretchable conductors based on buckled super-aligned carbon nanotube films. Nanoscale. 2015;7(22):10178–85.
[6] Qi D, Liu Z, Liu Y, Leow WR, Zhu B, Yang H, et al. Suspended wavy graphene microribbons for highly stretchable microsupercapacitors. Adv Mater 2015;27(37):5559–66.
[7] Choi DY, Kim MH, Oh YS, Jung S-H, Jung JH, Sung HJ, et al. Highly stretchable, hysteresis-free ionic liquid-based strain sensor for precise human motion monitoring. ACS Appl Mater Interfaces 2017;9(2):1770–80.
[8] Zhang X, Lin H, Shang H, Xu J, Zhu J, Huang W. Recent advances in functional fiber electronics. SusMat. 2021;1(1):105–26.
[9] Guo Q, Huang B, Lu C, Zhou T, Su G, Jia L, et al. A cephalopod-inspired mechanoluminescence material with skin-like self-healing and sensing properties. Mater Horiz 2019;6(5):996–1004.
[10] Liang J, Li L, Tong K, Ren Z, Hu W, Niu X, et al. Silver nanowire percolation network soldered with graphene oxide at room temperature and its application for fully stretchable polymer light-emitting diodes. ACS Nano 2014;8(2):1590–600.
[11] Wu X, Han Y, Zhang X, Zhou Z, Lu C. Large-area compliant, low-cost, and versatile pressure-sensing platform based on microcrack-designed carbon Black@polyurethane sponge for human-machine interfacing. Adv Funct Mater 2016;26(34):6246–56.
[12] Zhu C, Han TY-J, Duoss EB, Golobic AM, Kuntz JD, Spadaccini CM, et al. Highly compressible 3D periodic graphene aerogel microlattices. Nat Commun 2015;6(1):6962.
[13] Xu F, Wang X, Zhu Y, Zhu Y. Wavy ribbons of carbon nanotubes for stretchable conductors. Adv Funct Mater 2012;22(6):1279–83.
[14] Won Y, Kim A, Yang W, Jeong S, Moon J. A highly stretchable, helical copper nanowire conductor exhibiting a stretchability of 700%. NPG Asia Mater 2014;6(9):e132.
[15] Jing W, Zhou F, Gao W, Jiang Z, Ren W, Shi J, et al. Regulating the hydrothermal synthesis of ZnO nanorods to optimize the performance of spirally hierarchical structure-based glucose sensors. RSC Adv 2015;5(105):85988–95.
[16] Wu X, Han Y, Zhang X, Lu C. Spirally structured conductive composites for highly stretchable, robust conductors and sensors. ACS Appl Mater Interfaces 2017;9(27):23007–16.
[17] Liu Y, Zheng H, Liu M. High performance strain sensors based on chitosan/carbon black composite sponges. Mater Des 2018;141:276–85.
[18] Lin Y, Liu S, Chen S, Wei Y, Dong X, Liu L. A highly stretchable and sensitive strain sensor based on graphene-elastomer composites with a novel double-interconnected network. J Mater Chem C 2016;4(26):6345–52.
[19] Wang C, Pan ZZ, Lv W, Liu B, Wei J, Lv X, et al. A directional strain sensor based on anisotropic microhoneycomb cellulose nanofiber-carbon nanotube hybrid aerogels prepared by unidirectional freeze drying. Small. 2019;15(14):1805363.
[20] Liu D-S, Ryu H, Khan U, Wu C, Jung J-H, Wu J, et al. Piezoionic-powered graphene strain sensor based on solid polymer electrolyte. Nano Energy 2020;105610.
[21] Chen S, Song Y, Ding D, Ling Z, Xu F. Flexible and anisotropic strain sensor based on carbonized crepe paper with aligned cellulose fibers. Adv Funct Mater 2018;28(42):1802547.
[22] Li Y, Samad YA, Taha T, Cai G, Fu S-Y, Liao K. Highly flexible strain sensor from tissue paper for wearable electronics. ACS Sustainable Chem Eng 2016;4(8):4288–95.
[23] Yu X-G, Li Y-Q, Zhu W-B, Huang P, Wang T-T, Hu N, et al. A wearable strain sensor based on a carbonized nano-sponge/silicone composite for human motion detection. Nanoscale. 2017;9(20):6680–5.
[24] Gong S, Schwalb W, Wang Y, Chen Y, Tang Y, Si J, et al. A wearable and highly sensitive pressure sensor with ultrathin gold nanowires. Nat Commun 2014;5(1):3132.
[25] Shi J, Li X, Cheng H, Liu Z, Zhao L, Yang T, et al. Graphene reinforced carbon nanotube networks for wearable strain sensors. Adv Funct Mater 2016;26(13):2078–84.
[26] Zhang D, Xu S, Zhao X, Qian W, Bowen CR, Yang Y. Wireless monitoring of small strains in intelligent robots via a Joule heating effect in stretchable graphene-polymer nanocomposites. Adv Funct Mater 2020;30(13):1910809.
[27] Wei S, Fang X, Yang J, Cao X, Pintus V, Schreiner M, et al. Identification of the materials used in an Eastern Jin Chinese ink stick. J Cult Heritage 2012;13(4):448–52.
[28] Wang S, Cao Y, Zhang Q, Peng H, Liang L, Li Q, et al. New application of old material: Chinese traditional ink for photothermal therapy of metastatic lymph nodes. ACS Omega 2017;2(8):5170–8.
[29] Yang HC, Chen Z, Xie Y, Wang J, Elam JW, Li W, et al. Chinese ink: A powerful photothermal material for solar steam generation. Adv Mater Interfaces 2019;6(1):1801252.
[30] Zhou L, Sun L, Fu P, Yang C, Yuan Y. Carbon nanoparticles of Chinese ink-wrapped natural loofah sponge: a low-cost three-dimensional electrode for high-performance microbial energy harvesting. J Mater Chem A 2017;5(28):14741–7.
[31] Liu QC, Li L, Xu JJ, Chang ZW, Xu D, Yin YB, et al. Flexible and foldable Li-O_2 battery based on paper-ink cathode. Adv Mater 2015;27(48):8095–101.
[32] Wang H, Yang W, Cheng L, Guan C, Yan H. Chinese ink: High performance nanofluids for solar energy. Sol Energy Mater Sol Cells 2018;176:374–80.
[33] Yan W, Dasari A, Kong LB. Chinese ink-facilitated fabrication of carbon nanotube/polyvinyl alcohol composite sheets with a high nanotube loading. Compos A Appl Sci Manuf 2014;61:209–15.
[34] Lucci A, Turner RR, Morton DL. Carbon dye as an adjunct to isosulfan blue dye for sentinel lymph node dissection. Surgery. 1999;126(1):48–53.
[35] Cao Y, Song W, Jiang Q, Xu Y, Cai S, Wang S, et al. Nanoparticles from ancient ink endowing a green and effective strategy for cancer photothermal therapy in the second near-infrared window. ACS Omega 2020;5(11):6177–86.
[36] Eynard L, Laurière M. The combination of Indian ink staining with immunochemiluminescence detection allows precise identification of antigens on blots: application to the study of glycosylated barley storage proteins. Electrophoresis 1998;19(8–9):1394–6.
[37] Xiong Y, Zhu Y, Liu X, Zhu P, Hu Y, Sun R, et al. A flexible pressure sensor based on melamine foam capped by copper nanowires and reduced graphene oxide. Mater Today Commun 2020;24:100970.
[38] Du R, Gao X, Feng Q, Zhao Q, Li P, Deng S, et al. Microscopic dimensions engineering: Stepwise manipulation of the surface wettability on 3D substrates for oil/water separation. Adv Mater 2016;28(5):936–42.
[39] Zhang P, Wang R, He M, Lang J, Xu S, Yan X. 3D Hierarchical Co/CoO-graphene-carbonized melamine foam as a superior cathode toward long-life lithium oxygen batteries. Adv Funct Mater 2016;26(9):1354–64.
[40] Liang Q, Li Z, Yu X, Huang ZH, Kang F, Yang QH. Macroscopic 3D porous graphitic carbon nitride monolith for enhanced photocatalytic hydrogen evolution. Adv Mater 2015;27(31):4634–9.
[41] Lee JS, Park GS, Kim ST, Liu M, Cho J. A highly efficient electrocatalyst for the oxygen reduction reaction: N-doped ketjenblack incorporated into Fe/Fe_3C-functionalized melamine foam. Angew Chem Int Ed 2013;52(3):1026–30.
[42] Ruan C, Ai K, Li X, Lu L. A superhydrophobic sponge with excellent absorbency and flame retardancy. Angew Chem 2014;126(22):5662–6.
[43] Lin X, Chen J, Yuan Z, Yang M, Chen G, Yu D, et al. Integrative solar absorbers for highly efficient solar steam generation. J Mater Chem A 2018;6(11):4642–8.
[44] Xue F, Lu Y, Qi X-d, Yang J-h, Wang Y. Melamine foam-templated graphene nanoplatelet framework toward phase change materials with multiple energy conversion abilities. Chem Eng J 2019;365:20–9.
[45] Wu F, Pickett K, Panchal A, Liu M, Lvov Y. Superhydrophobic polyurethane foam coated with polysiloxane-modified clay nanotubes for efficient and recyclable oil absorption. ACS Appl Mater Interfaces 2019;11(28):25445–56.
[46] Branca C, Frusteri F, Magazu V, Mangione A. Characterization of carbon nanotubes by TEM and infrared spectroscopy. J Phys Chem B 2004;108(11):3469–73.
[47] Li D, Müller MB, Gilje S, Kaner RB, Wallace GG. Processable aqueous dispersions of graphene nanosheets. Nat Nanotechnol 2008;3(2):101–5.
[48] Ferrari AC, Basko DM. Raman spectroscopy as a versatile tool for studying the properties of graphene. Nat Nanotechnol 2013;8(4):235–46.
[49] Yuan X, Luo K, Zhang K, He J, Zhao Y, Yu D. Combinatorial vibration-mode assignment for the FTIR spectrum of crystalline melamine: A strategic approach toward theoretical IR vibrational calculations of triazine-based compounds. J Phys Chem A 2016;120(38):7427–33.
[50] Yuan X, Luo K, Wu Y, He J, Zhao Z, Yu D. Investigation on the stability of derivative melam from melamine pyrolysis under high pressure. Nanomaterials. 2018;8(3):172.
[51] Devallencourt C, Saiter J, Fafet A, Ubrich E. Thermogravimetry/Fourier transform infrared coupling investigations to study the thermal stability of melamine formaldehyde resin. Thermochim Acta 1995;259(1):143–51.
[52] Ma Z, Kang S, Ma J, Shao L, Wei A, Liang C, et al. High-performance and rapid-response electrical heaters based on ultraflexible, heat-resistant, and mechanically strong aramid nanofiber/Ag nanowire nanocomposite papers. ACS Nano 2019;13(7):7578–90.
[53] Ma Z, Kang S, Ma J, Shao L, Zhang Y, Liu C, et al. Ultraflexible and mechanically strong double-layered aramid nanofiber-$Ti_3C_2T_x$ MXene/silver nanowire nanocomposite papers for high-performance electromagnetic interference shielding. ACS Nano 2020;14(7):8368–82.
[54] Pan L, Chortos A, Yu G, Wang Y, Isaacson S, Allen R, et al. An ultra-sensitive resistive pressure sensor based on hollow-sphere microstructure induced elasticity in conducting polymer film. Nat Commun 2014;5(1):3002.

Support information

Chinese Ink Coated Melamine Foam with Joule Heating and Photothermal Effect for Strain Sensor and Seawater Desalination

Xiang Cao[a], Hongzhong Liu[a], Jiabing Cai[a], Linhong Chen[a], Xiya Yang[b], Mingxian Liu[a,*]

[a] Department of Materials Science and Engineering, Jinan University, Guangzhou 510632, China

[b] Institute of New Energy Technology, College of Information Science and Technology, Jinan University, Guangzhou 510632, PR China

*Corresponding author. Email: liumx@jnu.edu.cn

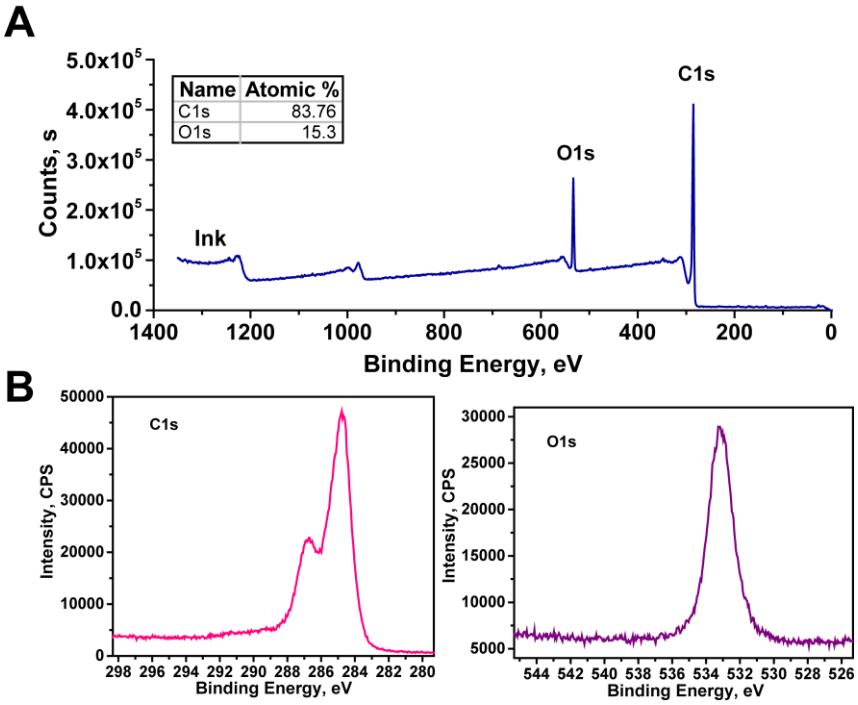

Fig. S1. The survey of (A) XPS spectra of ICN and (B) high resolution scanning of ICN.

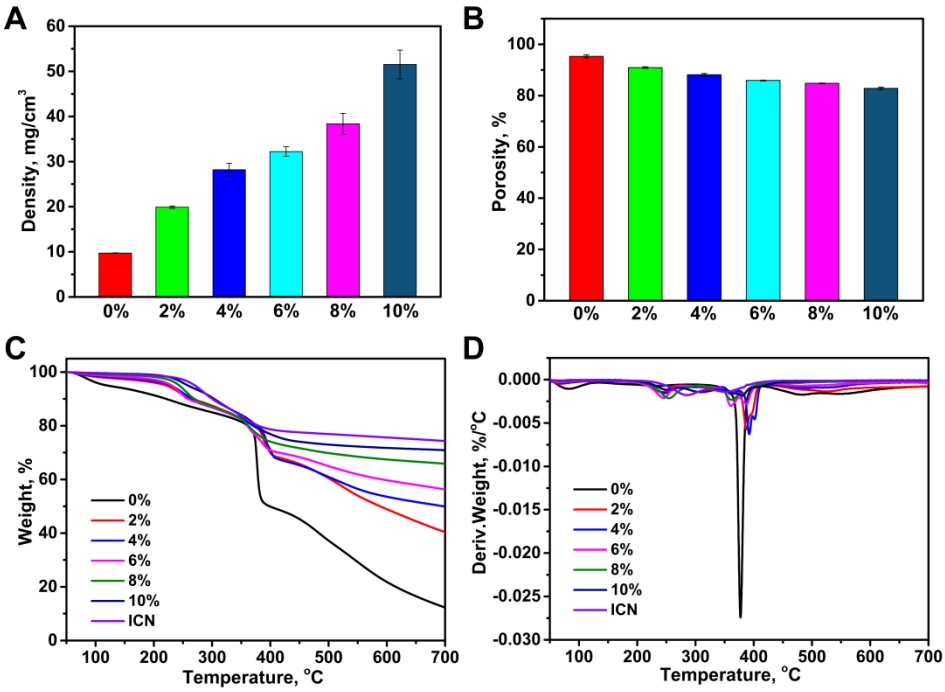

Fig. S2. (A) Density, (B) porosity, (C) thermogravimetric curves and (D) derivative thermogravimetric curves of CMF with different ICN contents and ICN.

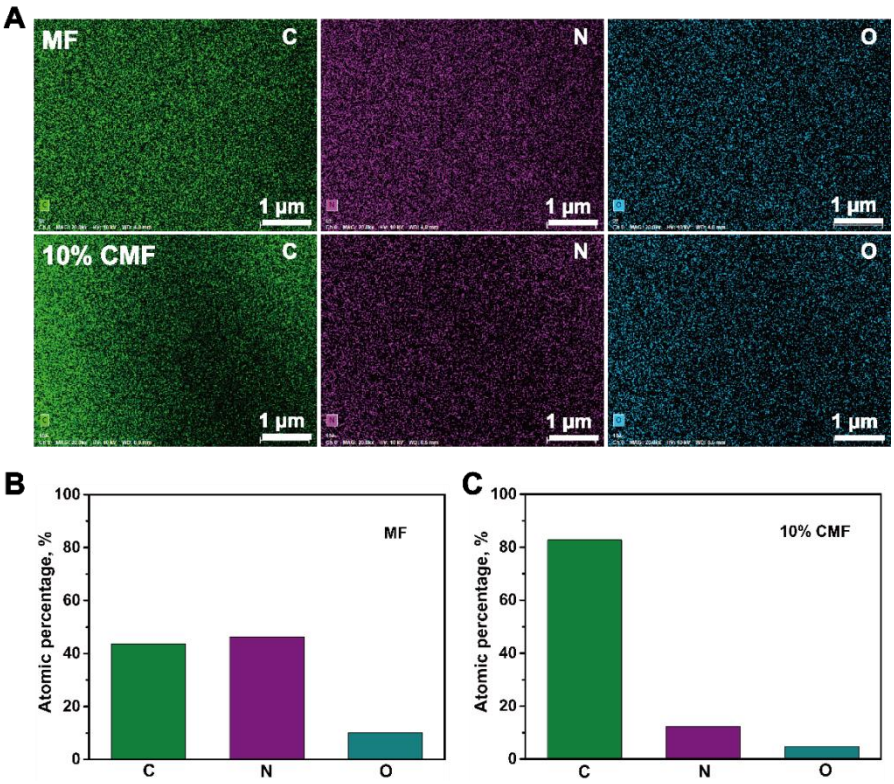

Fig. S3. (A) EDS elemental mapping and (B, C) atomic percentage of 0% and 10% CMF.

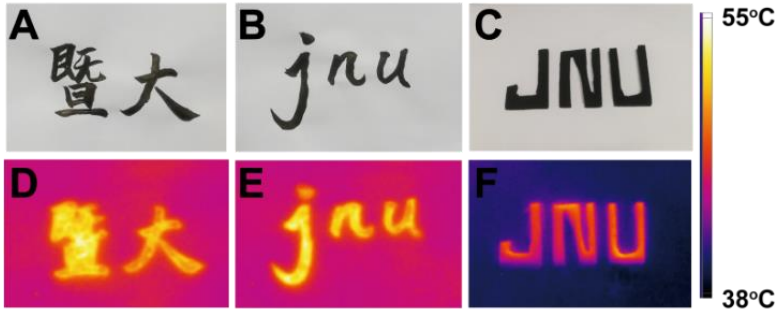

Fig. S4. Photographs and photothermal images of calligraphy and CMF.

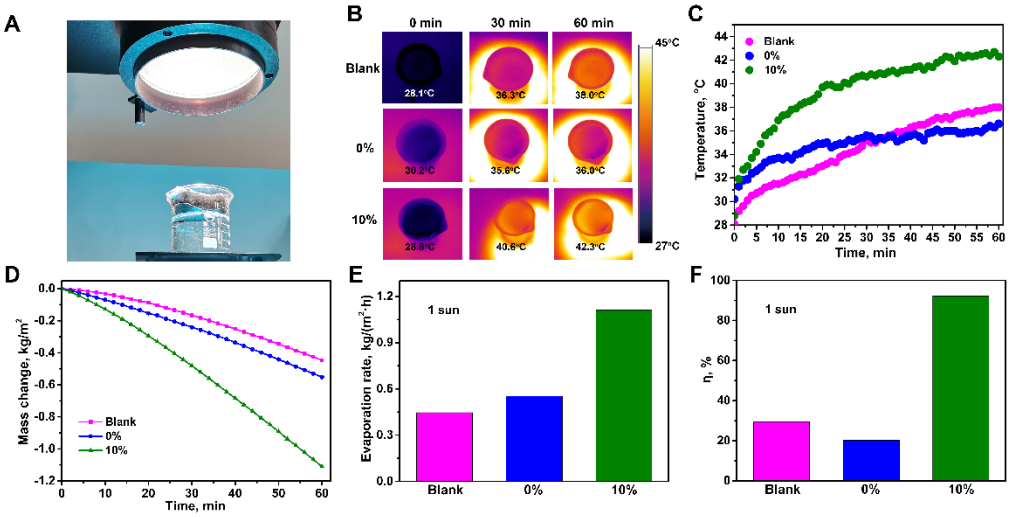

Fig. S5. Seawater evaporation behavior of the 10% CMF under irradiation of one sun. (A) Appearance of the device; (B) Photothermal images; (C) Temperature change of the sample with different ICN contents; (D) Mass change of water versus time; (E) Evaporation rate; (F) Evaporation efficiency.

We employed simulated sun light to carry out the seawater desalination. Fig. S5A shows the photo of desalination device under one sun light and three groups (blank, 0% and 10% CMF) were performed. Photothermal images are displayed in Fig. S5B, which provides obvious difference about surface temperatures. The surface temperature of 10% CMF increases to 42.3°C from 28.8°C within 60 min (Fig. S5C). In contrast, the surface temperature of pure foam and blank only reached 36.6°C and 38.0°C from 30.2°C and 28.1°C, respectively. The light reflection of white pure foam leads to low photothermal conversion ability which is even not as good as the blank sample. Fig. S5D shows the mass loss of the three groups. The 10% CMF shows rapider and more mass loss of seawater than other groups. The mass loss of blank, 0% and 10% CMF is 0.45, 0.55 and 1.11 kg/m^2, respectively. As expected, the evaporation rate (Fig. S5E) of 10% CMF is much higher than that of blank and 0%

CMF, and the evaporation efficiency (Fig. S5F) of 10% CMF is 92.24% which is much higher than that of blank (29.52%) and 0% CMF (20.34%). It also demonstrates that CMF can be an excellent photothermal material used in seawater desalination.

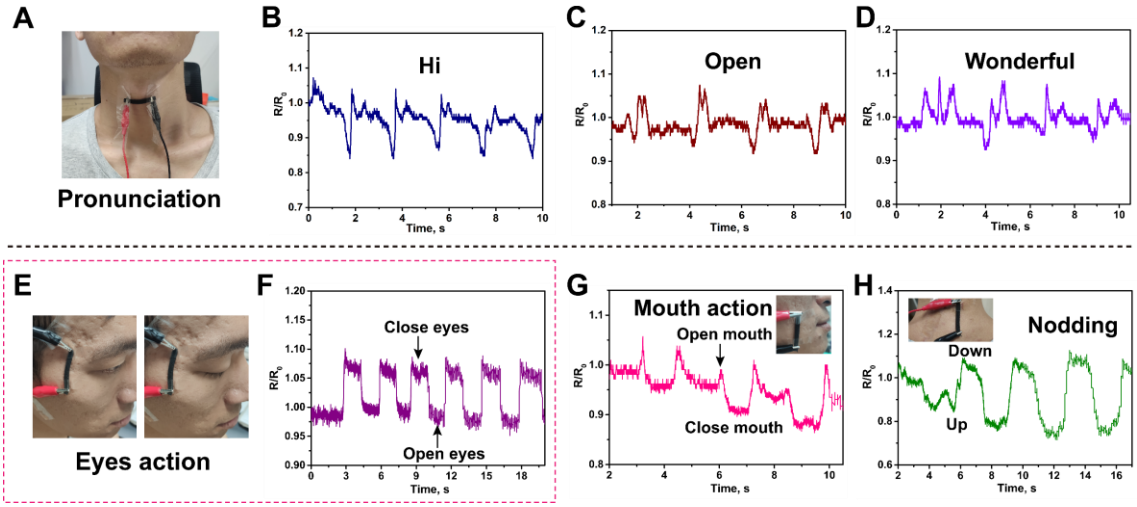

Fig. S6. Physiological monitoring application of the 10% CMF in (A-D) pronunciation, (E-F) eye action, (G) mouth action and (H) nodding.

In order to further investigate the ability of CMF acting as a strain sensor to monitor tiny human activity, the sample was employed to detect routine physiological actions of human body, such as pronunciation, eyes action, mouth action and nodding. Firstly, a CMF strip was attached to the throat of the volunteer (Fig. S6A) and various signals (Fig. S6B, C and D) were detected by speaking different words (such as hi, open and wonderful). The characteristic signal generated by the sensor is related with the different words because certain form of muscle motion in the throat, and the tiny strain is accurately transferred into a distinct electrical signal. This specific recognition property of pronunciation shows promising potential in speech recognition device. Afterwards, the CMF was fixed at other position of tester such as right side of eye, mouth corner and neck. The corresponding characteristic signals are

presented in Fig. S6E, F, G, H. These signals possess good repeatability and reliability. In conclusion, the CMF sensor is capable to monitor tiny movement of human body, which can be applied in the manufacture of smart device in healthcare equipment.